Utrecht University

Bachelor Thesis

Diffraction Full Field Imaging on Perovskite Samples

Author:
Eric van Bruggen

Supervisor:
Dr. Jan Hilhorst

July 29, 2015

Abstract

{ In this thesis a method to image organic inorganic hybrid perovskites using full field X-ray diffraction microscopy is introduced. Diffraction microscopy is used to image hybrid perovskites. It was found that lead halide perovskite solar cells show interesting structural behaviour under an applied voltage, which is evidence that structural relaxation might be the cause of the anomolous hysteresis observed in these structures }

Contents

Chapter 1

Introduction

"It is not often that the scientific community is blessed with a material, which brings enormous hopes and receives special attention. When it does, it expands at a rapid pace and its every dimension creates curiosity. One such material is perovskite." (From: Angewandte Chemie, Kazim 2014)[1]

Today, fossil fuels are dominating the electricity generation sector [2]. Today's society is a society where harmful gases, originating from exhaustible fuels are posing a large threat on climate and environment, oil prices are getting higher, and the political situation in the Middle-East with it's huge oil reserves is becoming increasingly unstable. The demand for renewable energy has never been higher than now. So, now would be a perfect time for an energy transition, and solar energy just might be the perfect candidate to replace fossil fuels. To make this transition, society asks a great deal of science. Cheap, eco friendly ways to harvest solar energy must be discovered, as current technologies either ask for large investments with a long payback time or are not economically viable at all [3]. Large scale solar energy harvesting seems to be a dream for the future. But now, we might have already found one of future's materials. We are talking about perovskites.

Perovskites are a class of materials that can be produced from cheap, abundant materials and production is easy and not cost-intensive. Interesting optic and electronic properties make perovskites very interesting for applications in photovoltaics, with recent publications already reporting on a solar cell with 17.9% power conversion efficiency (PCE). And development is going very fast. An important problem to address in order to achieve even higher power conversions is the appearance of a hysteresis effect in the I-V curves of hybrid perovskite solar cells. This effect makes it hard to obtain reliable power conversion efficiencies. A solid understanding of this hysteresis effect will lead to more reliable research and possibly to higher power conversion efficiencies. In this thesis, first a theoretic background will be given on perovskites, perovskite solar cells and the origin of the hysteresis effect. A method to clarify the origin of the hysteresis effect using X-ray diffraction full field imaging will be given and theoretically explained. With the help of obtained results, an answer will be formulated on the question: 'Can we elucidate the origin of the hysteresis effect of perovskite solar cells with full field diffraction microscopy?'

Chapter 2

Theory

2.1 Perovskite solar cells

2.1.1 General information

Perovskite was first discovered by Gustave Rose in 1839 in the mineral $CaTiO_3$. He named the material perovskite after the Russian mineralogist L.A Perovski, a famous and influential statesman at that time [4]. The general formula of perovskites can be described as ABX_3. Here X represents an anion, A a larger cation and B a smaller cation [5]. The crystal structure of perovskite is depicted in figure 2.1.

In 1954, the Danish scientist Christian Moller observed photo conductivity in metal halide perovskites and proved semiconducting behaviour of perovskite. 24 years later, Dieter Weber used methylammonium cations ($CH_3NH_3{}^+$) to synthesize the first organic-inorganic hybrid perovskite [6]. It then took a long time before the enormous potential of hybrid perovskites was recognized for use in photovoltaic applications. It was only in 2006 when Miyasiki *et al.* first reported on a hybrid perovskite solar cell [7]. From then on, research on perovskite flared up. Perovskite solar cells (PSCs) increased rapidly in efficiency. Six years ago (2009),

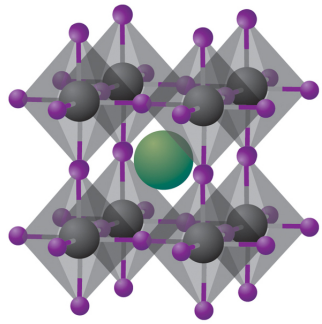

Figure 2.1: X(purple) represents an anion, A(green) a larger cation and B(grey) a smaller cation from (Gratzel M. 2014)[6]

the maximum PCE reported was still 3.8% [8]. Today, one can find PCE's well over 15% with a highest PCE reported at 17.9% [5]. Perovskites are in the centre of research interest. Only in 2015, already 1,866 articles about perovskites have been published [9] and much more are to be expected. As one could read in nature vol 13 (sep 2014) [10] "It is difficult to resist the intense appeal of hybrid organic-inorganic perovskites"

2.1.2 Electronic properties

The hype around hybrid perovskites can be easily justified because of the exceptionally promising electronic and optical properties for use in photovoltaic applications. In general, perovskites have wide direct band gaps which can be tuned by changing one of the components A, B or X. [1]

A typical and popular material in this class that attracts a lot of attention is methylammonium lead iodide ($CH_3NH_3PbI_3$). $CH_3NH_3PbI_3$ has a direct bandgap of 1.55 eV. This means an absorption onset at 800nm which makes $CH_3NH_3PbI_3$ a good light absorber over the whole visible solar emission spectrum. Perovskite combines this suitable absorption range with a high absorption coefficient [6]. Furthermore, perovskites such as $CH_3NH_3PbI_3$ tend to have ultra-fast exciton separation (picoseconds), high charge carrier mobilities and very slow exciton recombination (microseconds) which leads to electron-hole diffusion lengths of over 1 μm, very efficient charge collection, and ultimately high solar cell efficiency [11–13].

These interesting properties can be contributed to the large dielectric constant of $CH_3NH_3PbI_3$ (6.5), and thus delocalised Wannier-Mott type excitons with a large exciton bohr radius (22 $\mathring{A}$) and a low exciton binding energy (50meV) that is comparable to the thermal energy k_bT of 26 meV at room temperature [14, 15]. Electrons and holes that are formed when an electron is excited, have a small effective mass, about 0.15 m_0^* as a direct result of band structure of the $CH_3NH_3PbI_3$-perovskite [16] which is beneficial for the charge carrier mobility. [6, 16] Cl 'doping' can improve the charge transport even further [17].

2.1.3 Preparation of hybrid perovskite solar cells

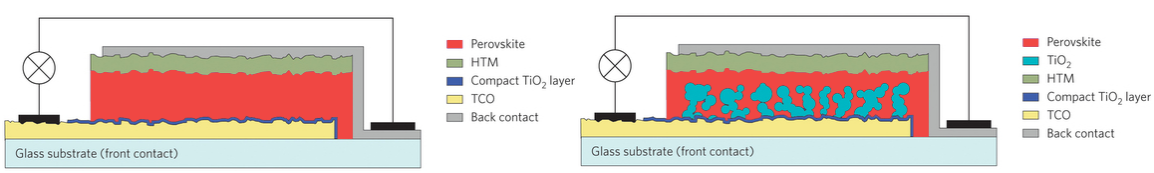

(a) (b)

Figure 2.2: (a) perovskite solar cell without TiO_2 scaffold and (b) perovskite solar cell with TiO_2 scaffold , reproduced from Gratzel M. (2014)[6]

In figure 2.2 a basic perovskite solar sell is shown. The key component is the perovskite light harvester. When a photon is absorbed by the perovskite, an electron is excited, creating

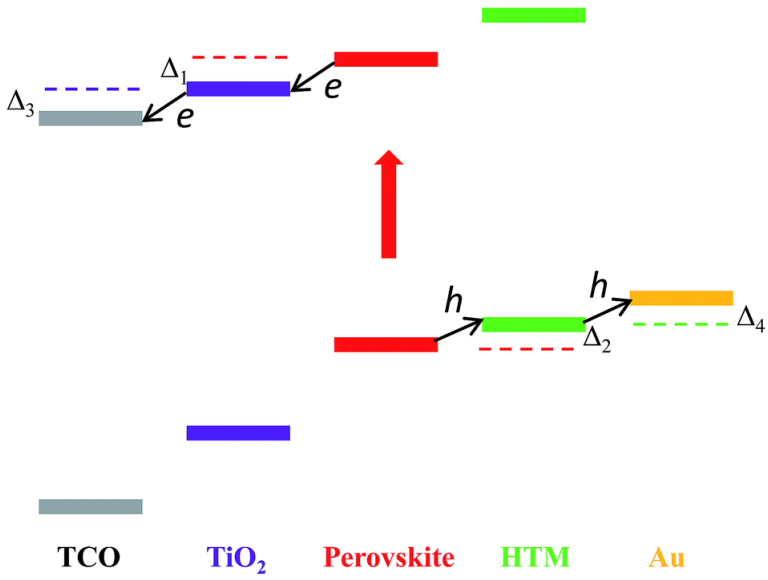

Figure 2.3: Energy band alignment of perovskite solar cells (Yin, 2015).[19]

an electron-hole pair. Holes diffuse to a suitable hole transporter material (HTM) such as spiro-OMeTAD from where they can reach a cathode (e.g. Au). On the other side of the perovskite excited electrons are transferred to an electron transporter material such as TiO_2 and are transported to a transparent conducting oxide (TCO) such as fluorine doped tin oxide (FTO) or indium tin oxide (ITO). All these layers are deposited on a glass substrate.

Important for the efficiency of a solar cell is the band gap design. In a traditional silicon solar cell, p and n-type doping are used to accurately change the energy levels of the silicon, and thus creating an efficient charge separation. In perovskite solar cells, using the right hole and electron transporters is of utmost importance. The energy of the conduction band (CB) of the electron transporter material (ETM) should be close in energy to the CB of the perovskite, and the HOMO of the HTM should almost match the HOMO of the perovskite. A higher HOMO would lead to a decrease in open circuit voltage and a lower HOMO would lead to a decrease in hole transport efficiency. The opposite is true for the CB energy of the ETM. A too low CB would lead to a decrease in open circuit voltage, while a too high CB would lead to a decrease in electron transport efficiency. [18]

To increase surface area with the electron transporter material and decrease average diffusion lengths, historically, mesostructured TiO_2 has been used as electron transporter. 2.2(b) However, it is found that TiO_2 causes a significant loss in efficiency and might be replaced by the insulating Al_2O_3 or, not be replaced at all[20] as shown in figure 2.2. Notice however that still a small TiO_2 hole blocking layer must be present.

Two general ways of preparing PSCs are the one-step deposition route and the sequential step deposition method. In the one step method as described by M. Lee et al.[21] a perovskite precursor is infiltrated into a porous oxide mesostructure through spincoating, and afterwards dried. Perovskite is formed through self-assembly.

In the sequential step process proposed by Julian Burschka *et al.* in a first step a lead iodide solution in DMF is spincoated onto a porous oxide mesostructure and in a second step a CH_3NH_3I solution in 2-propanol is added [22]. Compared to the one-step deposition route, sequential deposition offers a better control over structural morphology and has a larger reproducibility.

2.1.4 Pitfalls and challenges

Before PSCs are ready for large scale manufacturing, there are a number of problems to overcome. One such problem is stability. In order to compete with existing solar cell technologies, it is necessary that long term stability (20+ years) will be achieved. Under humid conditions and under exposure of ultraviolet radiation, Lead-iodide PSCs can degrade, lose CH_3NH_3I and form PbI_2 [23]. Stability is of even more importance since lead compounds are very toxic and harmful to the environment. Degradation into soluble lead salts therefore poses a serious threat. This problem might be circumvented by using non-toxic tin analogues. Up to now however, tin analogues have proven to degrade in an oxygen rich atmosphere and in order to successfully replace lead, this problem has to be addressed. [12]

2.2 Hysteresis

A problem that hinders research is the appearance of a strong hysteresis effect in the photocurrent-voltage curves taken from perovskite solar cells. The measured current is not only dependent on the applied voltage, but also on the direction in which the I-V scan is taken. I.e. the current depends also on the voltage applied several seconds ago, a capacitive effect. A I-V curve scan with increasing voltage (forward scan) usually gives a smaller current than a scan with decreasing voltage (backward scan) would give. This makes it difficult to predict what PCE would have been measured when a steady voltage was applied for a longer period of time [24]. Publications with PCE values that have not been certified do not always take into account hysteresis and are likely to overestimate the PCE. Up until now, little is known about the source of this hysteresis phenomenon and a more solid understanding could lead to better solar cells, or at least, better comparable results. [25]

By changing the substrate on which the perovskite is grown, Snaith *et al.* observed that the size of the hysteresis effect was dependent on the different contact materials. One of the proposed explanations given by Snaith *et al.* is that substrate-induced dielectric polarization due to the ferromagnetic properties of the lead iodide perovskite might be the cause of their observations. [26] This is confirmed by a paper of R. S. Sanchez *et al.*. A slow rearrangement process in perovskite solar cells was found by means of transient photo decay (TPD) and a correlation with volt-current hysteresis was observed. Here, dielectric polarizability of the perovskite is suggested as a possible base of this phenomenon. [27, 28]

In order to confirm this hypothesis, other methods of measuring are necessary. One such method could be full field x-ray diffraction microscopy.

2.3 Full field X-ray diffraction imaging

In X-ray full- field imaging through lens-based microdiffraction (XFILM), highly monochromatic, short wavelength X-rays are used to irradiate a relatively large area (100 x 100 μm) of a crystalline sample (compared to scanning techniques). The sample is tilted in order to fulfil the Bragg conditions[29].

$$n\lambda = 2dsin(\theta)^1 \tag{2.1}$$

A lens is used to focus the X-rays after diffraction to obtain a diffraction image of the sample. A set-up is shown in figure 2.4

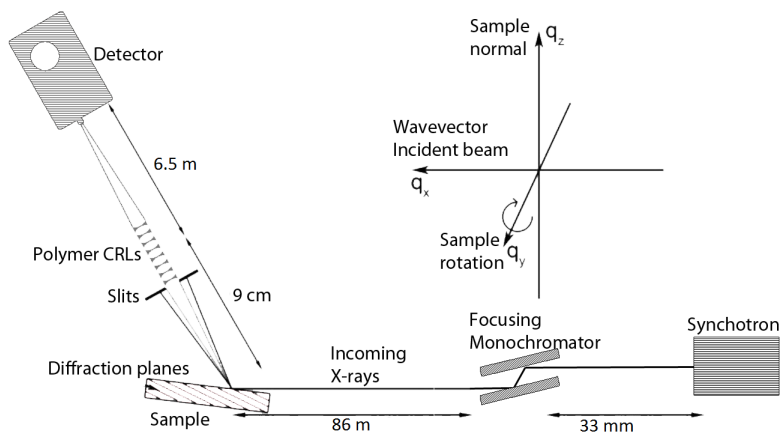

Figure 2.4: XFILM Setup, reproduced from Hilhorst(2014)[29]

2.3.1 Synchrotron light source

Highly monochromatic, short wavelength X-rays can be obtained by using a synchrotron light source. When charged particles are radially accelerated, electromagnetic radiation is produced. At a synchrotron light source, particles will be accelerated up to extremely high kinetic energies for which the radiation produced will be in the high energy X-ray range.

There are several synchrotrons around the world, specially designed to be used as an X-ray light source. One of the most powerful synchrotrons is the European synchrotron radiation facility light source (ESRF), located in Grenoble.

At the ESRF, electrons are first accelerated up to 200MeV in a linear accelerator, (Linac) before entering the circular booster synchrotron. Here, electrons are further accelerated up to 6 GeV after which they are stored into the storage ring. In a high vacuum ($10^{-9}mbar$), electrons can circulate at a constant energy for a longer period of time, i.e. several hours.

[1]Bragg's law with n the number of order, λ the wavelength, d the lattice spacing and θ the angle of incidence

The storage ring at the ESRF consists of 32 straight and curved sections. In the curved sections, bending magnets force the electrons into the right orbit. At the straight sections, focussing magnets ensure the straight path of the electrons. Undulators at the straight sections generate a brilliant beam of radiation. An undulator consists of periodically arranged dipole magnets that cause the electrons to oscillate. With the right periodicity, the X-rays emitted at each consecutive bend interfere constructively and a highly intense beam of X-rays is produced. See figure 2.6

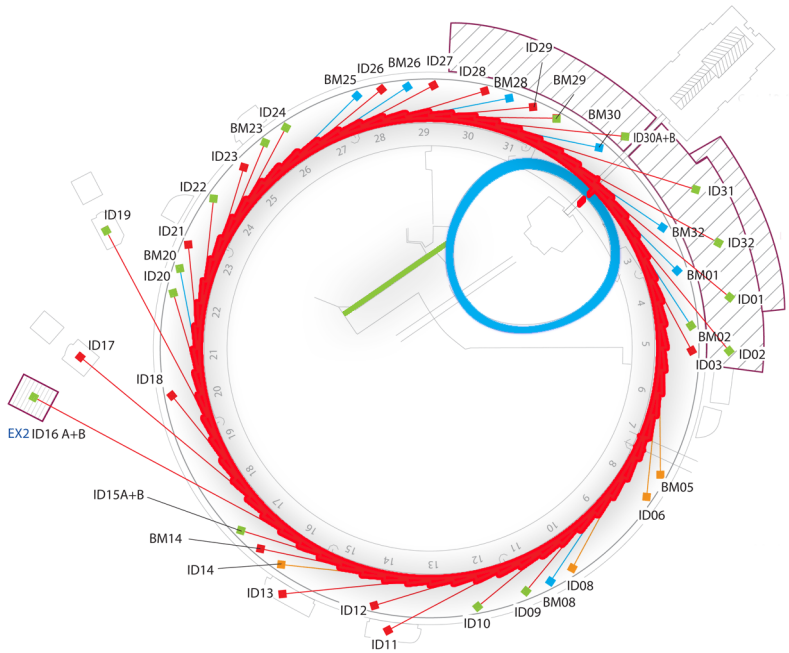

Figure 2.5: Synchotron at the ESRF. Every straight section produces highly energetic, bundled X-rays: a beamline. Green: Linac, blue: booster synchotron and red: storage ring. Original from esrf.fr [30]

2.3.2 X-ray optics

The X-rays coming from the undulator are monochromatized either by a $Si(111)$ monochromator or a multilayer monochromator. Monochromators use Bragg reflections in order to select X-rays with a certain wavelength. A monochromator made out of $Si(111)$ oriented crystals, has a well defined lattice spacing and a high resolution. A multilayer consists out of a stack of alternating thin layers and makes use of the different refractive indices of those layers to reflect the beam. Since the alternating layers are deposited periodically, the multilayer acts like a Bragg reflector. Compared to the $Si(111)$ monochromator, the multilayer has larger spacing d, a broader bandwidth and thus a higher photon flux. The $Si(111)$ monochromator however, has a better resolution.

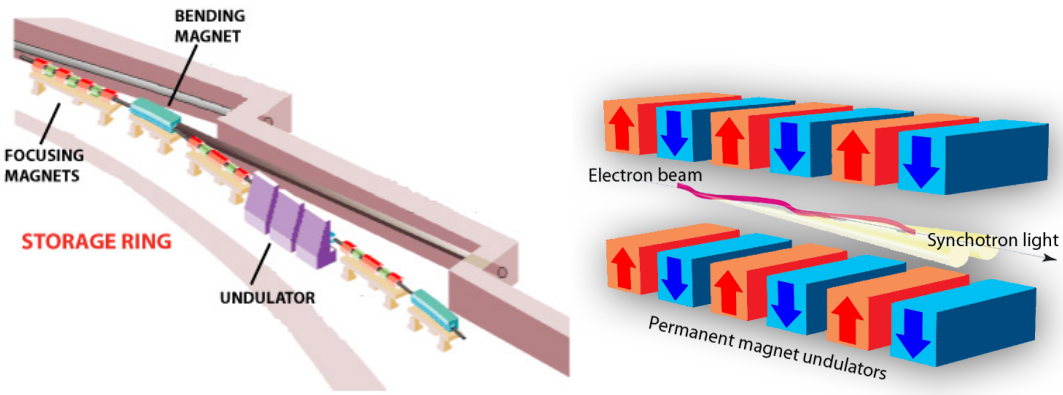

(a) (b)

Figure 2.6: (a) part of storage ring with (b) a schematic representation of an undulator. By periodically changing the magnet field, electrons are forced to oscillate and produce X-rays. Electrons are bend to the next straight section by bending magnets, X-rays propagate to a corresponding beam line. Original from esrf.fr[30]

Total reflection mirrors are placed before the monochromators to filter out the higher order wavelengths. This results in a highly brilliant X-ray beam of a single wavelength that can be used on a sample. [29]

Focussing an x-ray beam is a difficult task and was long thought not to be feasible. X-rays tend to be weakly refracted and strongly absorbed. It was in 1996 that Snigirev et al. first described a method to fabricate X-ray lenses. A compound refractive lens (CRL) was made by drilling closely spaced holes in aluminium.[31] Nowadays, multiple compound refractive lenses are available, most notably beryllium lenses and polymeric lenses. For microscopy, special lenses need to be produced and polymeric lenses might be the better choice. Beryllium lenses have a weaker absorption, but tend to be more polluted. Polymeric lenses have a larger refractive index, homogeneous background and are relatively cheap compared to beryllium.

2.3.3 Rocking curves

XFILM is a powerful method to quickly obtain diffraction images of a large region of interest (in the order of seconds). One can change the incidence angle gradually, by tilting the sample, in order to obtain rocking curves. Rocking curves plot the measured intensity against the angle of incidence. These rocking curves yield information about the lattice spacing d (2.1) calculated from the peak position and give a measure for the crystal size, calculated from the full width at half maximum (FWHM).

In XFILM, rocking curves can be calculated for every single pixel of the microscopy image. By fitting each of these curves an accurate rendering of Bragg peak positions, FWHM and integrated intensity per pixel can be given. Small differences in peak positions can tell

something about lattice strain or lattice tilts.

With the use of XFILM at perovskite samples, small differences in lattice spacing can be made visible in a matter of seconds. If lattice parameters change as a consequence of dielectric polarizability, this should appear in the results. Moreover, the time-scale in which XFILM can operate (tens of milliseconds) should be more than fast enough to do in situ measurements on the I-V hysteresis effect, an effect on the time-scale of (hundreds of) seconds. [26]

Chapter 3

Experimental

3.1 Sample preparation

For the voltage scans, mixed halide perovskite solar cell samples were prepared without a TiO_2-scaffold in a procedure based upon the solvent-induced fast crystallization-deposition method as described by Xiao *et al.* (2014)[32]. This method was chosen because of the large crystalline grains that can be produced using this method. A DMF solution of 0.23g $PbCl_2$ + 0.40g CH_3NH_3I in 1 ml of DMF corresponding to a molar ratio of 3 : 1 (MAI:PbCl2) was prepared and spin-coated upon an amorphous TiO_2-blocking layer, directly followed by addition of a non-solvent (chlorobenzene) to reduce solubility and induce crystallization. [32] See figure 2.2(a) for a cross-section. With this method, chloride ions are integrated in an amorphous lead-containing phase (sometimes incorrectly referred to as doped $MAPbI_3$ or $MAPbI_{3-x}Cl_x$[6, 17]). In this paper we will refer to this material as 'mixed halide perovskite'.

To align crystalline perovskites, in stead of an amorphous TiO_2-layer, oriented crystalline rutile TiO_2 was used, spincoated with $CH_3NH_3PbI_3$ but without other solar cell components such as glass, FTO or a HTM.

To determine the Bragg peak positions, complete solar cell samples were prepared following the two-step procedure described by Burschka *et al.* (2013) [22].

3.2 Bragg peak positions

In a set-up similar to the setup in fig 2.4, only without the lenses, that is, a normal X-ray diffraction set-up with a 20 keV X-ray beam, peak positions for a perovskite solar cell were detected at around 2 meters from the sample with a photon counting MAXIPIX detector system, developed by the ESRF . Comparison of these results with literature made it possible to assign peaks to the individual components of the perovskite solar cell (see appendix). Time scans were conducted to monitor possible degradation of the perovskite. This information was used in further experiments.

3.3 Voltage scan setup

Perovskite samples were placed in a nitrogen chamber. The samples were irradiated with a 20 keV X-ray beam, monochromatized by a Si(111) double bounce monochromator. At an incoming angle of 5.7 degrees, Bragg conditions for MAPbI perovskite were fulfilled. The diffracted light was focused by a set of SU-8 polymeric compound refractive lenses located at a distance of 10 cm from the sample. A vacuum tube was placed in between the lenses and the X-ray detector. An Andor Zyla 5.5 sCMOS detector with a pixel size of 6.5 microns was located 6.5 meters from the lens. The detector was used with a 200 μm thick Scint-X scintillator with a pore size of 25.7 μm that keeps contrast up to about 27 line pairs per millimetre (i.e. 37 μm per line pair) [33]. Together with an enlargement of 65x this results in a resolution of about 570 nm.

During measurements a voltage was applied over the solar cell. Forward scans, with increasing voltage from -1.0 V to 1.0 V and backward scans from 1.0 V to -1.0 V were taken in 42 steps total with an exposure time of 1 second. In between exposures, time was needed to process data, about 12 seconds. A complete back and forward scan of 42 steps took 580 seconds to complete. This was repeated for multiple positions on the perovskite sample.

In a second experiment, the incident angle of an 8 keV x-ray beam was changed every successive image in order to make rocking curves. The mixed halide lead iodide perovskite sample was put in Bragg conditions and tilted from 5.21°to 6.21°in 50 steps with an exposure time of 1 second each. To image the TiO_2 substrate, the sample was tilted to an incident angle of 18.84°to 18.94°in 100 steps of 10 seconds. This is around the angle corresponding to the (101) Bragg reflection of the TiO2 rutile substrate at 8 keV monochromated light. Beryllium lenses were used to focus the diffracted beam and full field microscopy images were obtained by the Andor detector.

3.4 Image processing

The images obtained from the Andor Zyla cannot be readily used and analysed. Image processing needs to be done before analysis can take place.

3.4.1 Background subtraction

Automatically the detector adds 100 counts intensity per pixel. These counts need to be subtracted. This can be easily done by writing a simple program. For this thesis, the programming language python was used to write the programs to perform the image processing.

3.4.2 Hot pixels

With the Andor one might encounter hot pixels. Hot pixels appear as unnaturally bright individual pixels in an image and are caused by leakage currents, especially at higher temperatures. They are visible at the same location in every image. This makes them easily

removable with software. A dark image, without x-ray radiation was taken and was used to assign hot pixels. In further image processing these known hot pixels were set to zero.

3.4.3 Noise reduction

Although the Andor detector has a relatively low noise level, noise was still very well visible. In general, setting a threshold intensity for signal and discarding everything below this threshold was enough to produce an almost noise free image. For images with a low signal intensity however, noise and signal were in the same range and more clever ways of noise reduction had to be applied.

To separate noise from signal, two criteria to determine noise were applied. 1) Noise is inconsistent in time. 2) Noise is equally distributed across the image and has no direct relation with neighbouring pixels. For the inconsistency cleaning operation, Andor images were compared with images taken before and after. Assumed was that the signal would remain in the same position. The counted values per pixel were multiplied for the three images (before, present and after), signal below a certain threshold was then removed and afterwards values were again divided by the values of before and after. This resulted in a fairly clean image, especially due to loss of noise by multiplying by zero.

Right after this 'inconsistency cleaning operation' a second rough approximation was applied. It was assumed that noisy pixels have no neighbours. For every pixel the values of the neighbouring pixels were checked. If all neighbouring pixels equalled zero, the signal was discarded as noise and set to zero.

3.4.4 Intensity correction

Since the intensity of the X-ray beam is not constant in time, a correction for intensity needs to be applied in order to compare results. Simply multiplying signal intensity by the current beam intensity divided by the initial beam intensity corrects for this fact.

3.4.5 Angle distortion correction

Because the Bragg reflections are imaged at small angles, microscopy images are distorted in one direction, resulting in a stretched view. To obtain non-stretched images, images are resized in one direction by a factor $1/sin(\nu - \phi)$ where ϕ is the incoming angle and ν the detector angle (see figure 3.1)

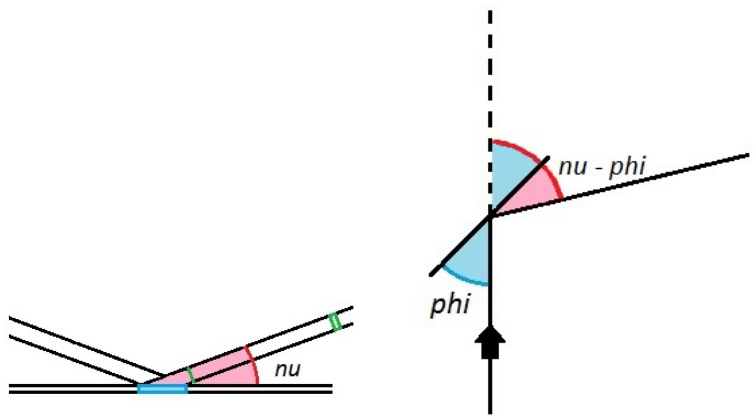

(a) (b)

Figure 3.1: (a) difference between size of the examined sample (blue) and size of the beam at the detector (in green) (b) Top view of set up with orientation of the angles. The blue area represents ϕ = incoming angle. The red and blue area together, indicated by the red line represent the detector angle ν. The red area represents ν - ϕ.

Chapter 4

Results and Discussion

4.1 XRD diffraction

High intensity peaks were found for different angles, which almost all could be assigned to one of the perovskite solar cell components. FTO, TiO_2, or $MAPbI_3$-Perovskite. A complete overview can be found in the appendix. At lower q-values, around 5, 9 and 17.5 nm^{-1} peaks showed up that did not match up with the expected spectra. This might be due to insufficient annealing of PbI_2. Several papers suggest that some kind of intermediate state might be responsible for these peaks.[34, 35] Remarkably during a time scan of 30 points, 10 seconds each, the precursor peaks seemed to gradually disappear, more rapidly than the perovskite peaks. This degradation is shown in figure 4.1. It is therefore unlikely that overall degradation of the sample is the cause of this decaying signal. Perhaps this could mean that under influence of the X-ray beam, annealing continues. Overall, the degradation rate of the perovskite was found to be slow enough to do measurements in the time scale of hundreds of seconds of exposure time. Long enough to perform rocking scans or take voltage scans.

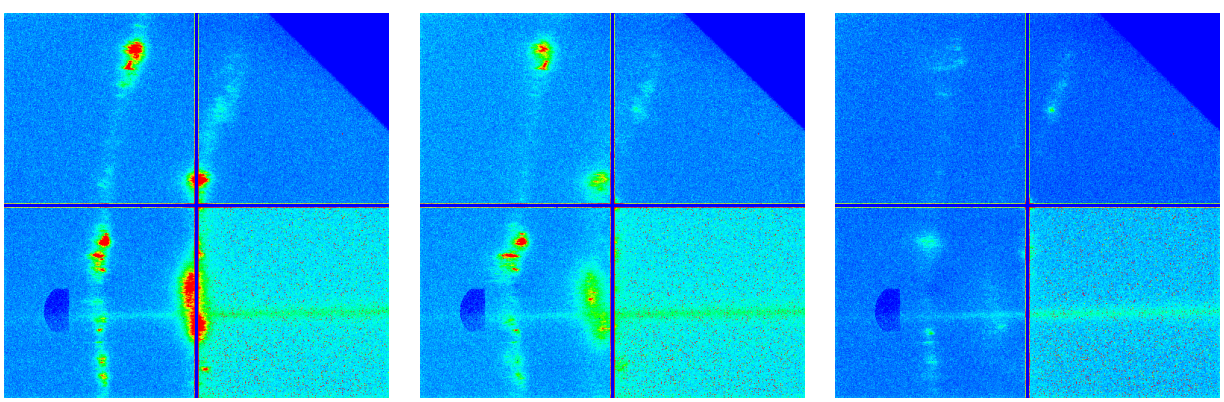

(a) (b) (c)

Figure 4.1: The appearance of a perovskite 'precursor' peak at the (a) start (0 sec) (b) middle (100 sec) and (c) end of a time scan (300 sec).

4.2 Imaging the substrate

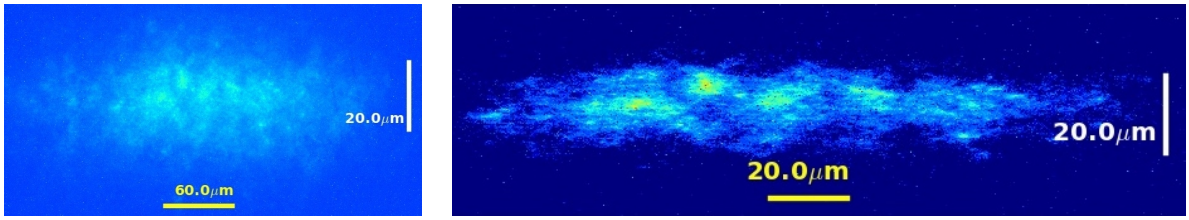

(a) (b)

Figure 4.2: (a) unprocessed image and (b) processed image of the TiO_2 substrate.

In figure 4.2 full field diffraction microscopy images of the TiO_2-substrate are shown with and without image processing. From the processed image, hot pixels were removed, the background was subtracted and the image was stretched to restore the real size proportions of the substrate. This was done for every image of the tilted sample, thirty in total and rocking curves per pixel were plotted and were fitted. From the rocking curves, integrals, peak positions and the full width at half maximum were calculated. In figure 4.3 results of the peak positions are shown.

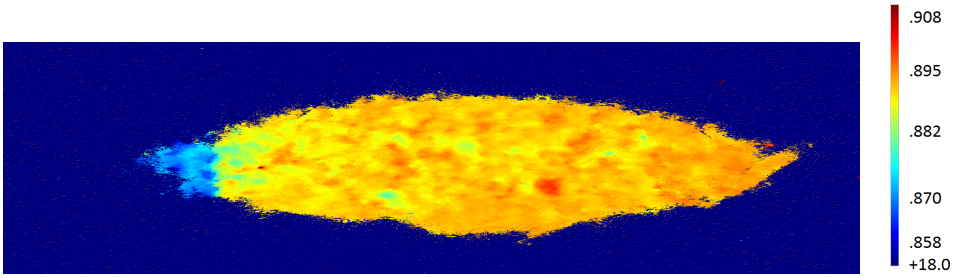

Figure 4.3: Peak positions of the rocking curves, calculated from XFILM images of the TiO_2-substrate. Colour indicates the angle of the peak position.

In figure 4.3, colour indicates the angle of the peak position of the rocking curve. Clearly visible is a domain at the left side of the image with peak positions at a lower angle. Different peak positions can indicate two things: variations in lattice spacing d or variations in lattice orientation. Without further research or knowledge on forehand, this cannot be assigned unambiguously with diffraction microscopy.

4.3 Imaging perovskite

Figure 4.4 shows a XFILM image of a mixed halide $CH_3NH_3PbI_3$ (220) plane for a tetragonal system at q = 20 nm^{-1} [21]. Around this q-value, a high intensity perovskite peak was seen

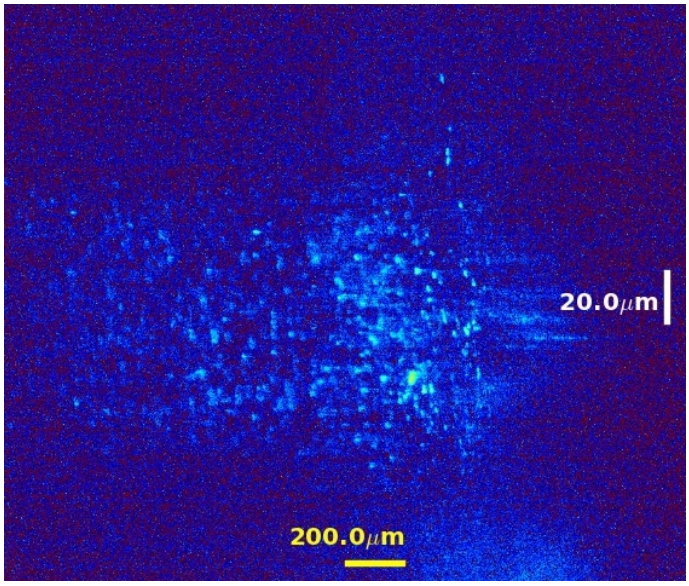

Figure 4.4: Full field diffraction microscopy image of perovskite

during earlier X-ray powder diffraction measurements and other than the (110) peak, a larger angle of incident can be used which yield better quality images. The domains are not continuously spread over the sample. We only see perovskite with a specific orientation, apparently this is not the same for every position at the sample. The same procedure that is used for the TiO_2-substrate can be used to obtain rocking curves for perovskite solar cells. Due to the small angles at which intense Bragg peaks of perovskite are found, the distortion factor due to imaging perovskite is large. In order to obtain real size proportions, the image should be stretched by a factor of more than 10 in the horizontal direction. As a consequence of this large factor, obtained figures are of inconvenient size, and difficult to analyse. Thus, in stead of applying this resize factor, images are kept the same size, but corrected relatively to each other for the incoming angle to make sure every pixel corresponds to the same sample position during the tilting of the sample for individual images.

In figure 4.5(a) the peak positions of the XFILM images taken around the (220) perovskite diffraction peak are plotted. Prominent is the presence of individual perovskite domains within the sample. This is in contrast with the continuous domains of the TiO_2-substrate (figure 4.3) and is caused by the different orientations of the perovskite domains. The full width at half maximum at figure 4.5(b) is a measure for the size of individual domains. There is a variety in FWHM visible, that indicates the presence of different domain sizes. The book-like shape visible in figure 4.5 (a) and (b) can be explained by the resize operation. Due to the resize operation, for every individual image, signal stays at the same pixel position, while noise and hot pixels do not, thus creating the line shaped noise in the background. Noise and hot pixels were not completely removed, because no advanced image processing has been done before creating the images in figure 4.5.

Figure 4.6 (a) and figure 4.6 (b) respectively show representative images of perovskite

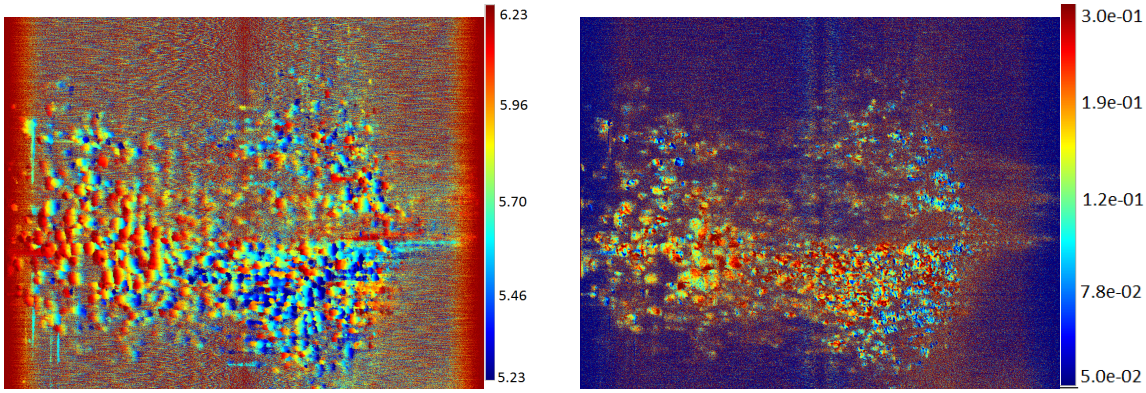

(a) peak positions (b) FWHM

Figure 4.5: (a) Peak positions and (b) Full width half maximum of the perovskite solar cell. Please keep in mind that the x-axis should in fact be stretched by a factor of 9.

during a voltage scan without and with noise reduction. During the voltage scans, the signal of the perovskites was generally very weak, and rigorous noise reduction has been applied such as described earlier in the experimental section. As is visible, the processed image is almost completely noise-free. For some examples signal seems to be lost together with noise, assumed is that this is a minor effect and that the benefit of increased noise reduction is larger than the drawback of loss in signal. Overall, processed images showed less fluctuations in signal and yielded more consistent outcomes compared to images with less rigorous noise reduction.

4.4 Voltage Scans

4.4.1 Overall decay

In figure 4.7 is the intensity of the signal plotted versus time. In a second line, the voltage applied to the solar cell is plotted. For every voltage scan, starting at 1 V, to -1 V and back to 1 V again, new coordinates on the sample are being examined. Despite changing the coordinates, the overall decrease in intensity clearly indicates degradation of the perovskite sample. Apparently, the change in coordinates was not large enough to overcome this problem. This result is backed up by a black 'burned' line that was visible on the sample after the X-ray experiments, adding up to the conclusion that the X-ray beam is responsible for the degradation of the PSC.

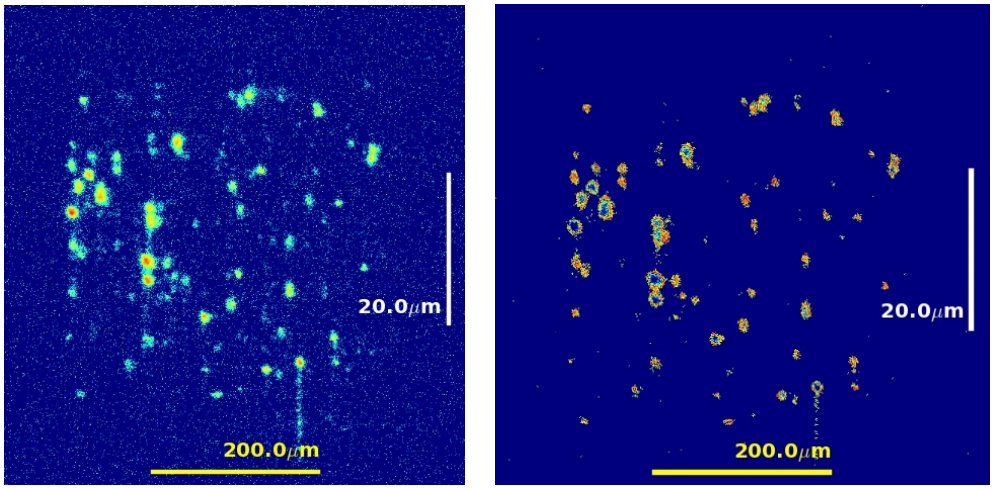

(a) (b)

Figure 4.6: (a) Perovskite image at an applied voltage of -1.0 V with (a) only backgroundsubtraction and (b) more advanced noise reduction.

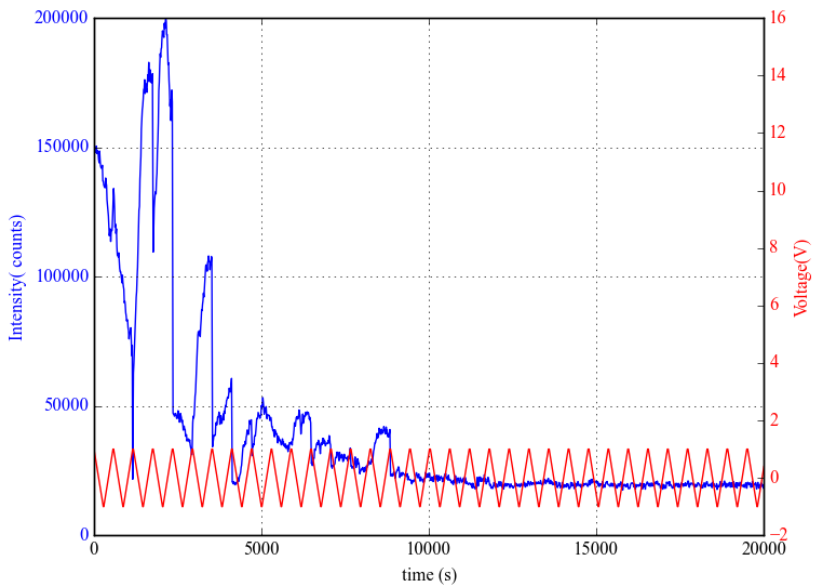

Figure 4.7: The intensity of the perovskite signal decays with time (blue). The red line show the applied voltage

4.4.2 Full Field Intensity

Figure 4.8 shows zoomed in selections from figure 4.7 . Each intensity measurement is made at a different positions on the sample. The images show different trends. Figure 4.8(a) shows an increase in intensity at decreasing voltage. Figure 4.8(b) shows a decreasing intensity at

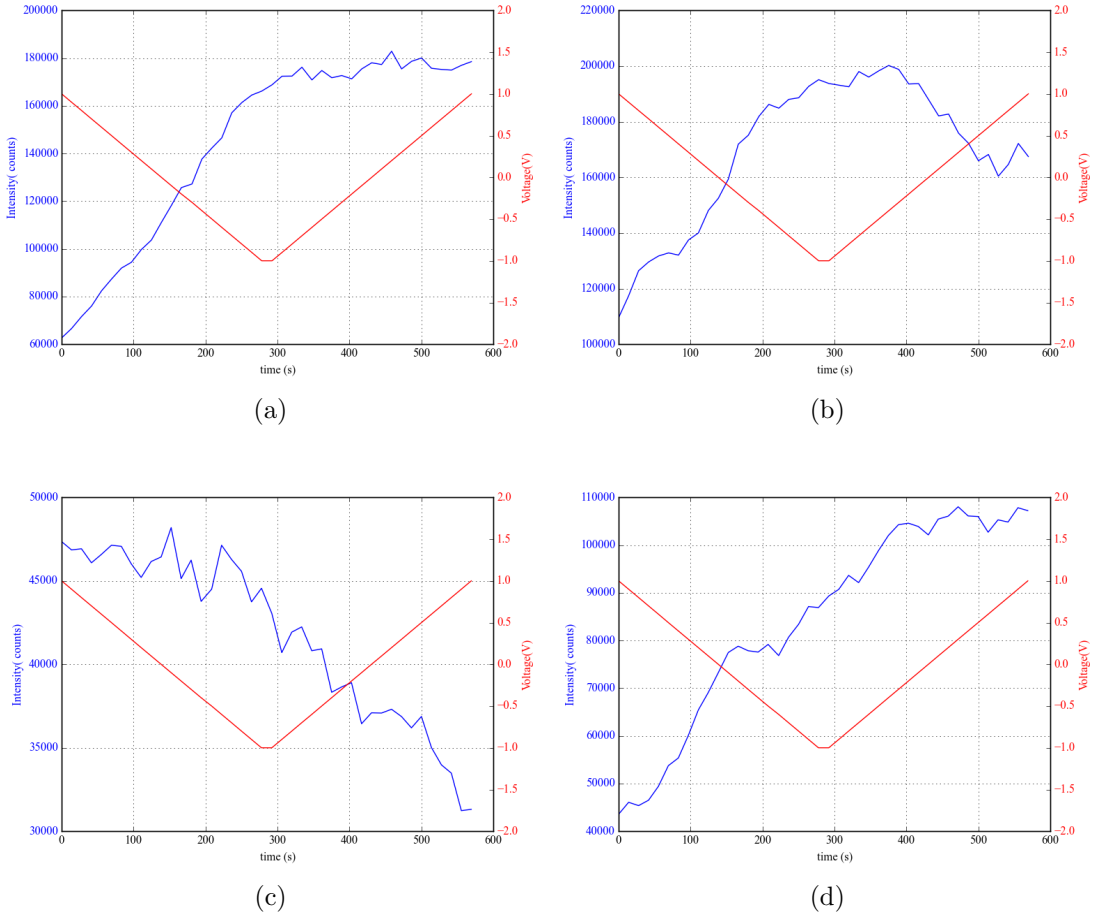

Figure 4.8: Intensity of the perovskite signal for different positions at the perovskite sample (blue), together with the applied voltage (red) .

increasing voltage. Figure 4.8(c) and 4.8(d) seem to be independent of the voltage. The intensity in figure 4.8(c) is decreasing in time while the intensity of figure 4.8(d) is increasing in time.

The different behaviour of the sample at different positions might be a consequence of different domains with different peak positions as shown in figure 4.5, moving in and out of Bragg conditions by structural changes.

4.4.3 Single Domain Intensity

To further test the hypothesis that a summation of intensity of different domains is responsible for the inconsequent graphs show in figure 4.8 , single domains were selected in the microscopy image. The possibility to select multiple single domains is one of the advantages of XFILM over other diffraction techniques. For these single domains, intensity was plotted

against time together with voltage in figure 4.9. From the voltage scan of 4.8 (a) different domains were selected, (e.g. 4.9(a)) and the intensity was again plotted together with the voltage. As is shown in figure 4.9 (b-f), for different positions in the diffraction microscopy image, the individual domains respond differently, with peak positions at different voltages. Summation of all domains would again lead to formation of the graph as shown in figure 4.8 (a). We notice increasing intensity over time in figure (b), (d), (e) and (f). Something that is very unlikely to be caused by degradation, or other effects from the x-ray beam, and therefore points to an effect of the applied voltage. A possible explanation is that, with an applied voltage, structural relaxation takes place due to alignment of dipolar domains to the electric field. This changing the lattice parameters of the perovskite, and causing a shift in the angle for which intensity is highest. Slight variations in peak position might be responsible for the shape of the graphs as shown in figure 4.9. One can however not completely rule out the effect of degradation on the peak positions of the perovskite domains. It might be possible that degradation of the PSC, leads to shifts in structural composition and tilt of individual domains, without decreasing their intensity. In a different experiment, not treated here, every voltage scan was repeated twice. Analysis of the data from this experiment might give valuable information about reproducibility and the effect of degradation. Combination of rocking scans with voltage scans could tell about the initial peak positions of the perovskite domains and whether and in what direction an applied voltage influences this peak positions. Future research on more stable PSCs could provide solutions to reduce the effects of degradation. Furthermore, growing perovskites in an oriented fashion would yield higher signal intensities for specific peaks and enable shorter exposure times.

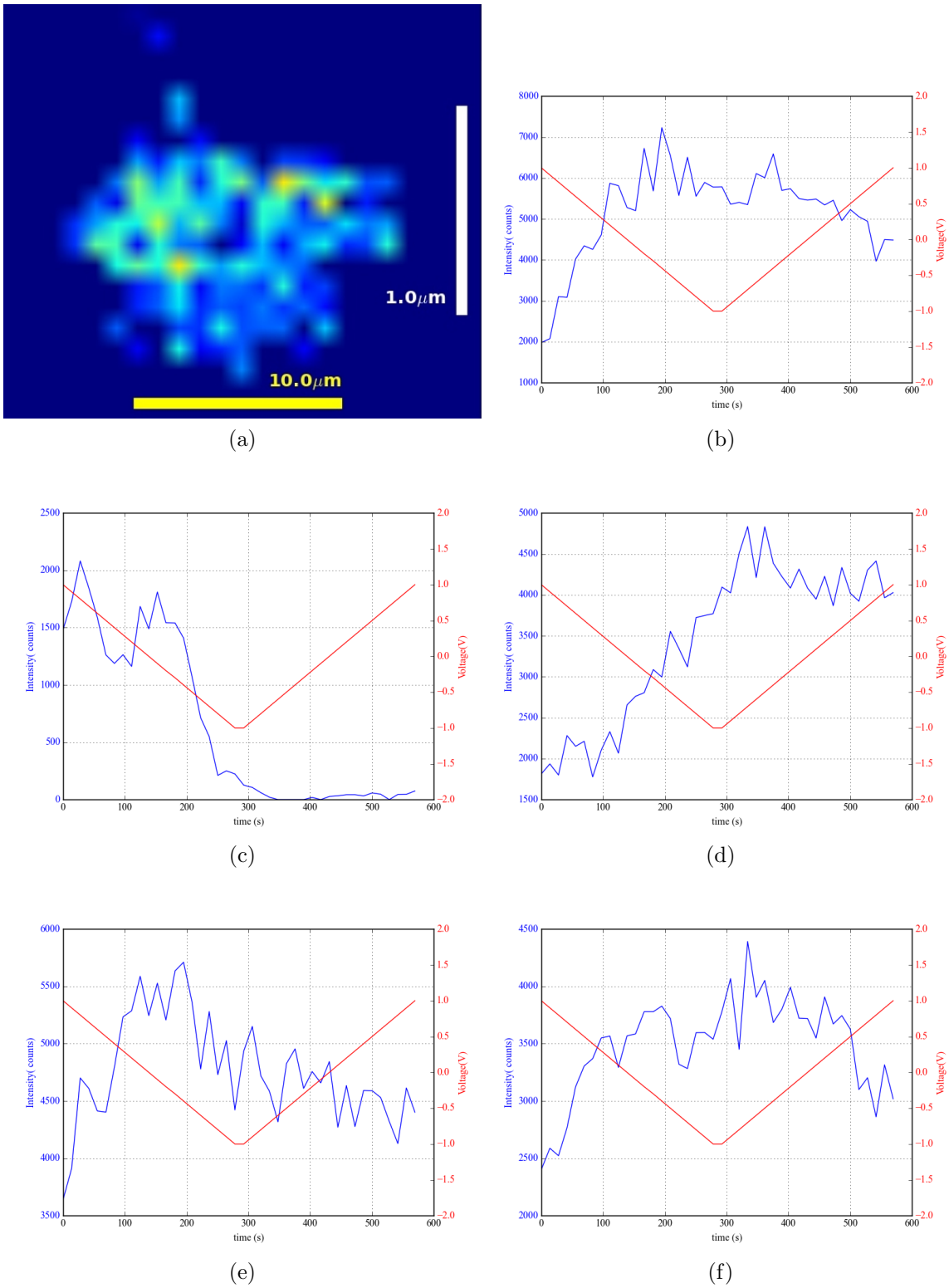

Figure 4.9: (a)Example of a microscopy image of a single domain of perovskite with (b) an intensity-voltage versus time graph for the domain shown at (a). (c-e) show graphs for different domains

Chapter 5

Conclusion

We used full field X-ray diffraction microscopy to image organic-inorganic perovskites. We found that $CH_3NH_3PbI_3$-perovskite degrades easily under influence of a high energy X-ray beam. Nevertheless, we showed that the use of XFILM could yield valuable information about structural properties of the latter, and that XFILM is able to image a large field of view, with the possibility to investigate specific domains . Evidence was found that structural relaxation due to dipolar alignment to the electric field takes place when a voltage is applied. Suggested is that this could be the origin of perovskite's hysteresis effect. The evidence however is not yet decisive. XFILM voltage scans on more stable perovskite solar cells combined with rocking curves might lead to a better understanding and conclusive evidence about the origin of the hysteresis effect.

Acknowledgements

This thesis would not have been possible without the help of the people at ID01 at the ESRF, Maria Mendez Malaga and Mathilde Bouchard of the LEMOH-group of Peter Reiss at the CEA who have prepared the perovskite samples, Andrei Petoukhov and Freddy Rabouw for giving me the opportunity to do my research at the ESRF and last but not least: Jan Hilhorst who supervised me during my research project.

Bibliography

1. Kazim, S., Nazeeruddin, M. K., Grätzel, M. & Ahmad, S. Perovskite as light harvester: A game changer in photovoltaics. *Angewandte Chemie - International Edition* **53,** 2812–2824. ISSN: 14337851 (2014).
2. Tzimas, E. & Georgakaki, A. A long-term view of fossil-fuelled power generation in Europe. *Energy Policy* **38,** 4252–4264. ISSN: 03014215 (2010).
3. Hosenuzzaman, M, Rahim, N. a., Selvaraj, J & Hasanuzzaman, M. Global prospects , progress , policies , and environmental impact of solar photovoltaic power generation. *Renewable and Sustainable Energy Reviews* **41,** 284–297. ISSN: 1364-0321 (2015).
4. Schmidt, L. *Tracking down the truth of perovski* 2011.
5. Green, M. a., Ho-Baillie, A. & Snaith, H. J. The emergence of perovskite solar cells. *Nature Photonics* **8,** 506–514. ISSN: 1749-4885 (2014).
6. Grätzel, M. The light and shade of perovskite solar cells. *Nature Materials* **13,** 838–842. ISSN: 1476-1122 (2014).
7. Kojima, A., Teshima, K., Shirai, Y. & Miyasaka, T. Novel Photoelectrochemical Cell with Mesoscopic Electrodes Sensitized by Lead-halide Compounds (11). *Meeting Abstracts* **2,** 27. ISSN: 2151-2043 (2008).
8. Kojima, A., Teshima, K., Shirai, Y. & Miyasaka, T. Organometal halide perovskites as visible-light sensitizers for photovoltaic cells. *Journal of the American Chemical Society* **131,** 6050–6051. ISSN: 00027863 (2009).
9. Webofscience.com. *Web of Science [v.5.17]* (visited on 07/07/2015).
10. Editorial. Perovskite fever. *Nature Materials* **13,** 837–837. ISSN: 1476-1122 (2014).
11. Ponseca, C. S. *et al.* Organometal halide perovskite solar cell materials rationalized: Ultrafast charge generation, high and microsecond-long balanced mobilities, and slow recombination. *Journal of the American Chemical Society* **136,** 5189–5192. ISSN: 15205126 (2014).
12. Hao, F., Stoumpos, C. C., Cao, D. H., Chang, R. P. H. & Kanatzidis, M. G. Lead-free solid-state organicinorganic halide perovskite solar cells. *Nature Photonics* **8,** 489–494. ISSN: 1749-4885 (2014).
13. Gonzalez-pedro, V. *et al.* General Working Principles of CH 3 NH 3 PbX 3 Perovskite Solar Cells. *Nano Lett.* **14,** 888893 (2013).

14. Kim, H. S., Im, S. H. & Park, N.-g. Organolead Halide Perovskite : New Horizons in Solar Cell Research. *J. Phys. Chem. C* **118,** 56155625 (2014).

15. Sum, T. C. & Mathews, N. Advancements in Perovskite Solar Cells: Photophysics behind the Photovoltaics. *Energy & Environmental Science* **7,** 2518–2534. ISSN: 1754-5692 (2014).

16. Brivio, F., Butler, K. T., Walsh, A. & Van Schilfgaarde, M. Relativistic quasiparticle self-consistent electronic structure of hybrid halide perovskite photovoltaic absorbers. *Physical Review B - Condensed Matter and Materials Physics* **89,** 1–6. ISSN: 1550235X (2014).

17. Colella, S. *et al.* MAPbI3-xClx mixed halide perovskite for hybrid solar cells : the role of chloride as dopant on the transport and structural properties. *Chemistry of Materials* **25,** 4613 (2013).

18. Yang, Z. & Zhang, W.-H. Organolead halide perovskite: A rising player in high-efficiency solar cells. *Chinese Journal of Catalysis* **35,** 983–988. ISSN: 18722067 (2014).

19. Yin, W.-J., Yang, J.-H., Kang, J., Yan, Y. & Wei, S.-H. Halide perovskite materials for solar cells: a theoretical review. *J. Mater. Chem. A* **3,** 8926–8942. ISSN: 2050-7488 (2015).

20. Snaith, H. J. Perovskites : The Emergence of a New Era for Low-Cost , High-Efficiency Solar Cells. *J. Phys. Chem. Lett* **4,** 36233630. ISSN: 1948-7185 (2013).

21. Lee, M. M., Teuscher, J., Miyasaka, T., Murakami, T. N. & Snaith, H. J. *Efficient Hybrid Solar Cells Based on Meso-Superstructured Organometal Halide Perovskites* 2012. doi:`10.1126/science.1228604`.

22. Burschka, J. *et al.* Sequential deposition as a route to high-performance perovskite-sensitized solar cells. *Nature* **499,** 316–319. ISSN: 1476-4687 (2013).

23. Niu, G. *et al.* Study on the stability of CH3NH3PbI3 films and the effect of post-modification by aluminum oxide in all-solid-state hybrid solar cells. *Journal of Materials Chemistry A* **2,** 705. ISSN: 2050-7488 (2014).

24. McGehee, M. D. Perovskite solar cells: Continuing to soar. *Nature Materials* **13,** 845–846. ISSN: 1476-1122 (2014).

25. Noel, N. K. *et al.* Enhanced Photoluminescence and Solar Cell Performance via Lewis Base Passivation of Organic À Inorganic Lead Halide Perovskites. *ACS Nano* **8,** 9815–9821 (2014).

26. Snaith, H. J. *et al.* Anomalous hysteresis in perovskite solar cells. *Journal of Physical Chemistry Letters* **5,** 1511–1515. ISSN: 19487185 (2014).

27. Sanchez, R. S. *et al.* Slow dynamic processes in lead halide perovskite solar cells. Characteristic times and hysteresis. *Journal of Physical Chemistry Letters* **5,** 2357–2363. ISSN: 19487185 (2014).

28. Wei, J., Zhao, Y, Li, H, Li, G. & Pan, J. Hysteresis Analysis Based on Ferroelectric Effect in Hybrid Perovskite Solar Cells. *The Journal of Physical Chemistry Letters* **5,** 39373945 (2014).

29. Hilhorst, J., Marschall, F., Tran Thi, T. N., Last, a. & Schülli, T. U. Full-field X-ray diffraction microscopy using polymeric compound refractive lenses. *Journal of Applied Crystallography* **47,** 1882–1888. ISSN: 1600-5767 (2014).

30. ESRF. *esrf.fr/technologies* 2015. <`www.esrf.fr`>.

31. Snigirev, A., Kohn, V., Snigireva, I. & Lengeler, B. A compound refractive lens for focusing high-energy X-rays. *Nature* **384,** 49–51. ISSN: 0028-0836 (1996).

32. Xiao, M. *et al.* A Fast Deposition-Crystallization Procedure for Highly Efficient Lead Iodide Perovskite Thin-Film Solar Cells. *Angewandte Chemie - International Edition* **3169,** 1–7. ISSN: 14337851 (2014).

33. Http://www.scint-x.com/. *Scintillator - Scint-X Structured Scintillators* <`http://www.scint-x.com/`> (visited on 06/29/2015).

34. Tan, K. W. *et al.* Thermally Induced Structural Evolution and Performance of Mesoporous Block Copolymer Directed Amumina Perovskite Solar Cells. *ACS Nano* **8,** 4730–4739 (2015).

35. Moore, D. T. *et al.* Crystallization Kinetics of OrganicInorganic Trihalide Perovskites and the Role of the Lead Anion in Crystal Growth. *Journal of the American Chemical Society* **137,** 2350 –2358. ISSN: 0002-7863 (2015).

Appendix

Table 5.1: Perovskite solar cell X-ray Diffraction peaks

Angle() at 20 keV	**q(nm-1)**	**Angle (rad)**	**Obervations**	**Assignment**
1.5	5.31	0.03	double	Precursor
2.6	9.20	0.05	double	Precursor
2.975	10.52	0.05	strong	Perovskite
4	14.14	0.07	weak	Perovskite
5	17.67	0.09	very weak	Precursor /Perovskite/TiO2
5.325	18.81	0.09	strong	FTO
5.75	20.31	0.10		Precursor/perovskite
6.5	22.95	0.11		
6.75	23.83	0.12		FTO
7.6	26.81	0.13	strong	FTO/TiO2
10.125	35.64	0.18	strong	FTO
10.75	37.81	0.19	weak	TiO2
12	42.15	0.21		FTO
12.75	44.74	0.22		